Cell

Self-Organization of MTOCs Replaces Centrosome Function during Acentrosomal Spindle Assembly in Live Mouse Oocytes

Melina Schuh[1] and Jan Ellenberg[1,*]
[1] Gene Expression Unit, European Molecular Biology Laboratory (EMBL), Meyerhofstrasse 1, D-69117 Heidelberg, Germany
*Correspondence: jan.ellenberg@embl.de
DOI 10.1016/j.cell.2007.06.025

SUMMARY

Chromosome segregation in mammalian oocytes is driven by a microtubule spindle lacking centrosomes. Here, we analyze centrosome-independent spindle assembly by quantitative high-resolution confocal imaging in live maturing mouse oocytes. We show that spindle assembly proceeds by the self-organization of over 80 microtubule organizing centers (MTOCs) that form de novo from a cytoplasmic microtubule network in prophase and that functionally replace centrosomes. Initially distributed throughout the ooplasm, MTOCs congress at the center of the oocyte, where they contribute to a massive, Ran-dependent increase of the number of microtubules after nuclear envelope breakdown and to the individualization of clustered chromosomes. Through progressive MTOC clustering and activation of kinesin-5, the multipolar MTOC aggregate self-organizes into a bipolar intermediate, which then elongates and thereby establishes chromosome biorientation. Finally, a stable barrel-shaped acentrosomal metaphase spindle with oscillating chromosomes and astral-like microtubules forms that surprisingly exhibits key properties of a centrosomal spindle.

INTRODUCTION

Female meiotic spindles lack centrosomes in many species, including *Drosophila*, *C. elegans*, *Xenopus,* chicken, mice, humans, and all other mammals so far analyzed (Manandhar et al., 2005). Using live cell confocal microscopy, acentrosomal spindle assembly has been analyzed in *Drosophila* (Skold et al., 2005) and *Xenopus* oocytes (Gard, 1992). However, spindle assembly in mammalian oocytes has so far only been observed at relatively low temporal and spatial resolution (Dumont et al., 2007; Sorensen, 1973) so that chromosome and microtubule dynamics could not be analyzed quantitatively. The specific course of assembly is therefore still unknown (Brunet and Maro, 2005).

Much of the evidence for current mechanistic models of centrosome-independent spindle assembly comes from experiments performed in *Xenopus* egg extracts. In this cell-free system, functional bipolar spindles can form around DNA-coated beads in the absence of centrosomes (Heald et al., 1996), and they differ from mitotic spindles in that they are barrel shaped and lack astral microtubules and oscillating chromosomes (Desai et al., 1998; Maddox et al., 2003). The GTP-bound form of the small G protein Ran is proposed to drive assembly of such spindles by promoting chromosomal microtubule nucleation (Bastiaens et al., 2006; Caudron et al., 2005; Kalab et al., 2006). However, the importance of chromatin-mediated microtubule nucleation for meiotic spindle assembly in vivo remains to be tested, as a recent study suggests that Ran is not required to form the first meiotic spindle in both mouse and *Xenopus* oocytes (Dumont et al., 2007). Also, vertebrate oocytes contain acentriolar microtubule organizing centers (MTOCs) that may substitute centrosomes during acentrosomal spindle assembly.

Little is known about the nature and function of meiotic MTOCs. In mouse, they contain the pericentriolar material components γ-tubulin (Gueth-Hallonet et al., 1993; Palacios et al., 1993) and pericentrin (Carabatsos et al., 2000), but their developmental origin is controversial (Calarco, 2000; Can et al., 2003; Mattson and Albertini, 1990), and their microtubule nucleation properties are unknown. Different numbers of MTOCs have been observed, and different populations of MTOCs have been suggested to participate in the process of spindle assembly (Combelles and Albertini, 2001; Maro et al., 1985; Messinger and Albertini, 1991; Van Blerkom, 1991), but their function during spindle assembly has not been established. In vivo studies are therefore necessary to understand how exactly meiotic spindles form and whether spindle assembly relies on chromatin-mediated microtubule nucleation, the action of multiple acentriolar MTOCs, or a combination of both.

In this study, we have used 4D confocal fluorescence microscopy to quantitatively analyze the functional dynamics of single MTOCs, bivalent chromosomes, and microtubule plus ends during the entire process of acentrosomal

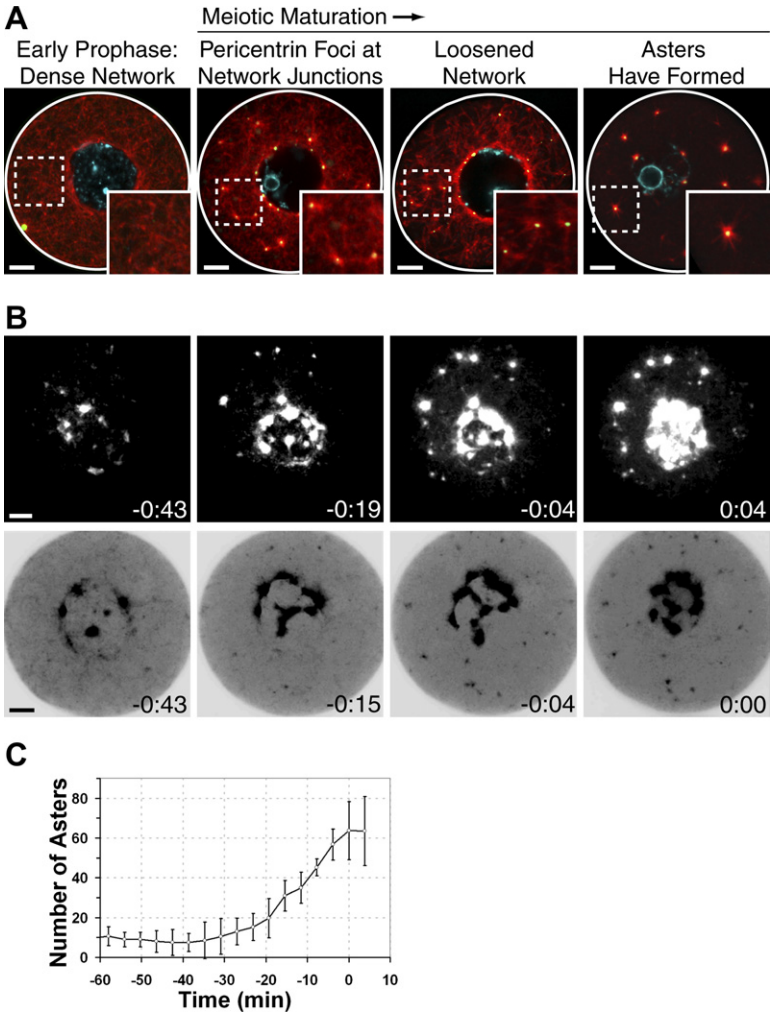

Figure 1. MTOCs Form De Novo from a Dense Interphase-like Microtubule Network

(A) Immunofluorescence of oocytes fixed at different times after oocyte isolation (first two panels: 0 min, third panel: 35 min, fourth panel: 50 min after isolation). Z-projection (three confocal sections, every 1.5 μm) of microtubules (red), chromosomes (blue), and pericentrin (green). Pericentrin signal appears yellow where it colocalizes with microtubules. Insets show magnified microtubule organization. Oocytes in early and late prophase were discriminated by their chromatin configuration: in early prophase, the chromatin fills the whole nuclear volume; in late prophase, the chromatin forms clusters at the nuclear envelope and around the nucleolus (Mattson and Albertini, 1990). The white circle marks the oocyte surface. Scale bar is 10 μm. See also Movie S1.

(B) Z-Projection (33 confocal sections, every 2.4 μm) of two different oocytes with larger, less numerous (upper panel) or smaller, more numerous MTOCs (lower panel) expressing EGFP-MAP4 (microtubules) during early maturation. The oocyte in the lower row is displayed inverted to highlight small MTOCs. Scale bar is 10 μm. Time, hh:mm relative to NEBD.

(C) Number of cytoplasmic asters plotted over time during early oocyte maturation as determined from 4D data sets of oocytes expressing EGFP-MAP4 (33 confocal sections, every 2.4 μm, Z stacks recorded every 231 s). Averages and standard deviations from four independent experiments are shown. See also Figure S1.

spindle assembly at high spatial and temporal resolution. Based on our data, we propose a new model of acentrosomal spindle assembly that relies on the self-organization of numerous acentriolar MTOCs, which functionally replace centrosomes. We show that MTOCs center at the nucleus, where they contribute to a Ran-dependent massive increase of the number of microtubules after nuclear envelope breakdown (NEBD), promote chromosome bivalent individualization, and progressively cluster into a bipolar spindle through the activity of kinesin-5.

RESULTS

MTOCs Form De Novo from a Dense Interphase-like Microtubule Network

To address the biogenesis of MTOCs in mouse oocytes, we analyzed the distribution of microtubules and pericentrin by 3D immunofluorescence from early to late prophase and during meiotic maturation. In early prophase, oocytes contained a dense interphase-like microtubule network with one to three cytoplasmic pericentrin foci (Figure 1A, first panel; Movie S1). In late prophase, microtubule density decreased slightly, and additional pericentrin foci appeared at network junctions and on the nucleus (Figure 1A, second panel; Movie S1). During meiotic maturation, microtubule network density diminished further (Figure 1A, third panel; Movie S1), while microtubule numbers increased locally at pericentrin foci, so that just before NEBD, the microtubule network had been replaced by many asters of variable size (Figure 1A, fourth panel; Movie S1). In summary, the vast majority of MTOCs forms de novo from a cytoplasmic microtubule network in prophase.

To measure the kinetics of aster formation, we recorded 4D data sets of microtubules labeled with MAP4-EGFP (Olson and Olmsted, 1999) in live oocytes (Figure 1B). In the first 30 min after onset of maturation, only 9 ± 5 asters were present in the cytoplasm (Figures 1C and S1; n = 4 oocytes). Subsequently, their number increased to 64 ± 15 at NEBD. In addition, approximately 10 to 25 asters were associated with the nuclear envelope (Figures 1B and S1) so that on average ~80 microtubule asters were present in mouse oocytes at NEBD consistent with immunofluorescence analysis of endogenous microtubules (Movies S1 and S2).

MTOC Microtubule Nucleation Is Similar to that of Centrosomes

To address whether the MTOCs have similar functional properties as centrosomes, we measured the growth and nucleation rates of MTOC microtubules using the plus-end marker EB3-mEGFP (Stepanova et al., 2003) in the cytoplasm and at the nucleus before and immediately after NEBD (Figure S2). Kymograph analyses revealed that MTOC-nucleated microtubules grew with a velocity of ~21 μm/min independent of their position or time relative to NEBD (Figure S2), well within the range reported for mitotic centrosomes (12–40 μm/min; Belmont et al., 1990; Hayden et al., 1990; Rusan et al., 2001; Srayko et al., 2005).

The nucleation rate of single MTOCs was proportional to MTOC size, averaging 49 ± 13/min before (n = 7) and 64 ± 30/min immediately after NEBD (n = 6), similar to the numbers reported for mitotic centrosomes in prophase and prometaphase (~60 /min; Piehl et al., 2004). Thus, mouse oocyte MTOCs have very similar microtubule nucleation properties as centrosomes, suggesting that they can substitute their function.

Cytoplasmic and Perinuclear MTOCs Cluster between Chromosomes after NEBD

Next, we wanted to determine whether only perinuclear or also cytoplasmic MTOCs contribute to spindle assembly. Tracking cytoplasmic MTOCs revealed that they relocated from periphery to center of the oocyte, where they participated in spindle assembly (Figures 2A–2C; Movie S3). Most MTOCs moved in a stop-and-go directional manner with velocities around 0.4 μm/min, although peak velocities up to 3.8 μm/min were observed (Figure S3). These dynamics are consistent with microtubule motors pulling MTOCs to the nuclear envelope or attracting MTOCs to each other. Our tracking data provide evidence for both mechanisms. First, MTOCs moved directly toward the nucleus, pushed against the nuclear envelope, and caused invaginations (Figures S4 and S2A; Movie S4), resulting in a microtubule network surrounding the nucleus (Figure 2D, panel 1; Movie S2). Second, overlapping microtubules connected cytoplasmic and perinuclear MTOCs (Figure 2D, panel 2; Movie S2) as well as cytoplasmic MTOCs (Figure 2D, panel 3; Movie S2). Third, MTOCs moved toward each other and formed larger MTOC clusters independent of the nucleus (Figure 2E). Overall, the nucleus (or chromosomes after NEBD) was the site of highest MTOC concentration in the oocyte, explaining the centripetal nature of MTOC movements. Interestingly, cortical microtubule contacts were often maintained during MTOC relocation (Figure 2D, panel 4; Movie S2), suggesting that cortical repulsion could contribute to MTOC centering.

Microtubules Are Predominantly Nucleated from MTOCs during Early Spindle Assembly

Next, we investigated whether in mouse oocytes microtubules are predominantly nucleated at chromosomes, similar to acentrosomal spindle assembly in *Xenopus* egg extracts, or at MTOCs, similar to centrosomal spindle assembly in mitotic cells. By labeling single microtubule plus ends and chromatin, we could measure the amount of microtubules relative to chromosomes. Before NEBD, the nuclear envelope was probed but not penetrated by microtubules originating from MTOCs (Figures 3A, time −0:49, and S5, before NEBD). In the first 24 ± 10 min (n = 14) after NEBD, microtubule plus ends were neither enriched on the chromatin surface nor moved away from chromosomes, indicating that chromosomal nucleation does not account for microtubules formed during early spindle assembly (Figure 3A, time 0:00–0:08). Immunofluorescence analysis of endogenous microtubules and chromosomes after NEBD confirmed that microtubules are predominantly found at MTOCs but not on the surface of chromosomes at this stage (Figure S5, at NEBD and after NEBD). During later spindle assembly, MTOCs clustered into a multipolar microtubule ball in close proximity to chromosomes, precluding to spatially distinguish microtubule nucleation at MTOCs or chromosomes (Figures 3A, time 0:25–1:22, and S5, chromosomes and MTOCs mix; Movie S5).

After NEBD, Microtubule Number Increases Massively in a Ran-Dependent Manner

Next, we used plus-end labeling of microtubules to analyze their number over time (Figure 3B, control). Quantitation revealed that microtubules were depleted rapidly from the cytoplasm while their number increased ~35-fold around MTOC clusters at chromosomes by 25 min after NEBD (Figure 3C), when nucleation could still be clearly attributed to MTOCs. This corresponds to more than 2000× the number of microtubules present on individual cytoplasmic MTOCs (Figure 3C, purple curve) and can therefore not be due to clustering of the ~80 preformed cytoplasmic MTOCs but instead represents de novo nucleation by the centering MTOCs. The exact correlation with NEBD suggested that the increase in microtubules is triggered by the release of nuclear factors. We therefore tested the requirement of Ran-GTP by injecting oocytes with purified RanT24N, which blocks Ran-GTP production by sequestering Ran's guanine nucleotide-exchange factor, RCC1, in an inactive, stable complex (Klebe et al., 1995). At a more than 4-fold excess over the estimated endogenous concentration (see Experimental Procedures), RanT24N prevented nuclear import in prophase-arrested oocytes, indicating that it efficiently inhibited Ran-GTP production (Figure S6). In maturing RanT24N-injected oocytes, the number of microtubules did not increase for ~2 hr after NEBD (Figures 3B and 3D, green curve) while mock-injected cells showed the massive increase after NEBD (Figure 3D, purple curve), which is therefore Ran dependent.

After an ~2 hr delay, however, the number of microtubules increased slowly in RanT24N-injected oocytes and allowed the formation of a spindle that contained less than half as many microtubules as in control oocytes (Figures 3D and S6C). Given the large excess of Ran T24N

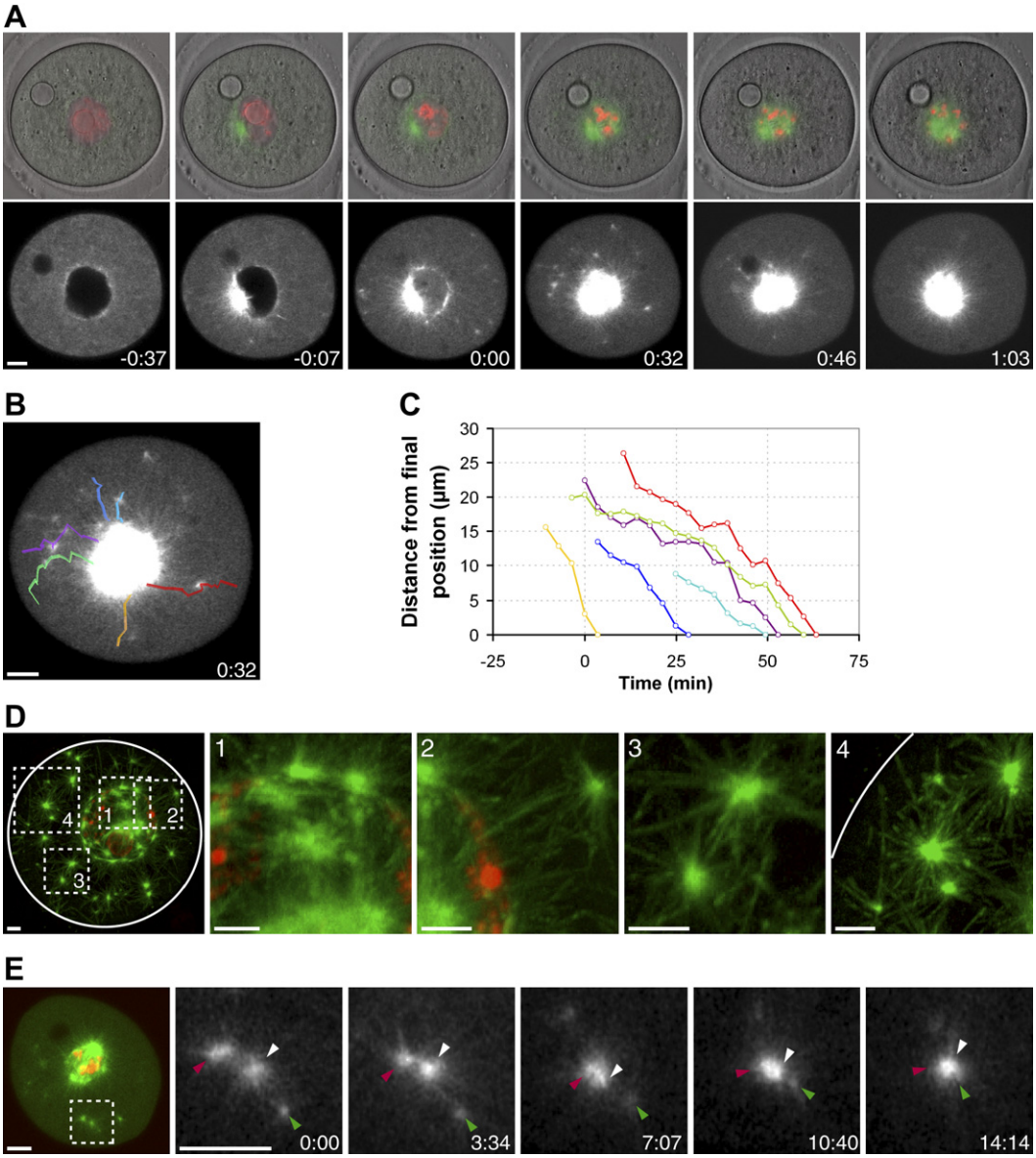

Figure 2. MTOCs Move Centripetally after NEBD and Interact with Each Other

(A) Time-lapse imaging of MTOCs in live mouse oocytes expressing EGFP-MAP4 (green, microtubules) and H2B-mRFP1 (chromosomes, red) merged with DIC images (upper panel). The EGFP-MAP4 signal (lower panel) was contrast and brightness adjusted to visualize cytoplasmic MTOCs. The black sphere visible in the cytoplasm is an oil droplet resulting from the microinjection procedure. Scale bar is 10 μm. Time, hh:mm relative to NEBD. See also Movie S3.

(B) MTOC tracks for the data set shown in (A) superimposed on EGFP-MAP4 signal (microtubules). Scale bar is 10 μm. Time, hh:mm relative to NEBD.

(C) Distances of MTOCs from their final position in the MTOC cluster plotted over time, calculated from (B).

(D) Immunofluoresence of an oocyte after complete aster formation just prior to NEBD. Z-projection (30 confocal sections, every 0.3 μm) of microtubules (green) and chromosomes (red). Microtubule connections between MTOCs on the nucleus (box 1), MTOCs on the nucleus and in the cytoplasm (box 2), two cytoplasmic MTOCs (box 3), and between MTOCs and the cortex (box 4) are highlighted, and the corresponding areas are shown magnified. The white circle marks the oocyte rim. Scale bar is 5 μm. See also Movie S2.

(E) Imaging of cytoplasmic MTOCs in live mouse oocytes expressing EGFP-MAP4 (green, microtubules) and H2B-mRFP1 (red, chromosomes). Colored arrowheads highlight relative positions of three MTOCs. Time, mm:ss. Scale bar is 10 μm.

we used and the efficient block of nucleocytoplasmic transport, it is unlikely that residual Ran-GTP drove this delayed increase in microtubule number. More likely this represents a second, Ran-independent phase of microtubule nucleation. To test whether it requires nuclear factors, we enucleated oocytes at different times after onset

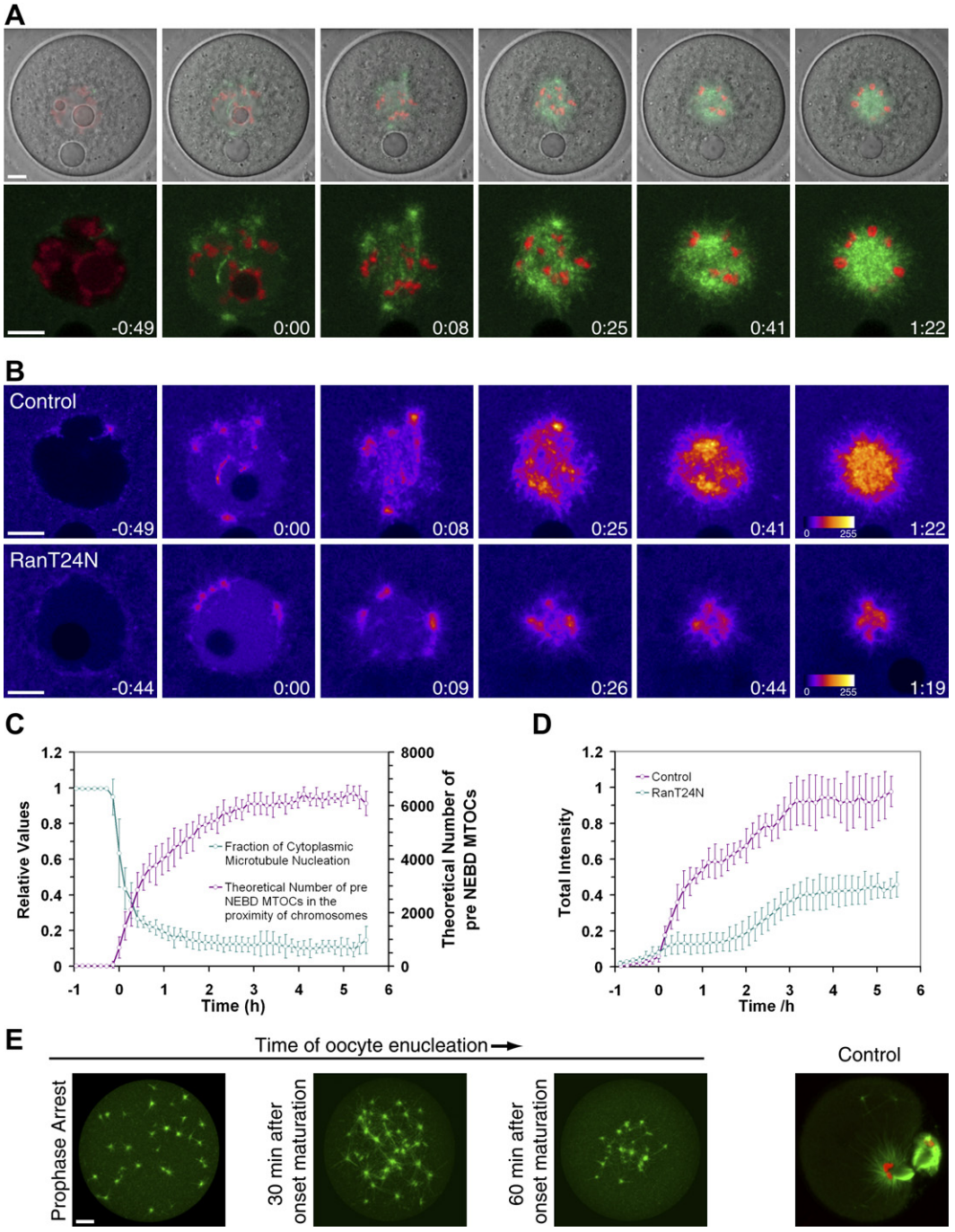

Figure 3. A Ran-Dependent Massive Increase in Microtubule Number after NEBD

(A) Time-lapse imaging of a maturing oocyte expressing EB3-mEGFP (microtubule plus ends, green) and H2B-mRFP1 (chromosomes, red) merged with DIC (upper panel) and magnified (lower panel). The sphere in the cytoplasm visible in the DIC channel is an oil droplet resulting from the microinjection procedure. Scale bar is 10 μm. Time hh:mm relative to NEBD.

(B) Pseudocolor representation of EB3-mEGFP signal in control (upper panel) or RanT24N-injected oocytes (lower panel). The corresponding look-up table is shown as a bar (last panels). Scale bar is 10 μm. Time hh:mm relative to NEBD.

(C) The theoretical number of preNEBD MTOCs that correspond to the actual number of microtubules in a 7 μm radius around the chromatin (purple curve) was determined from oocytes expressing EB3-mEGFP and H2B-mRFP1 like in (A). In addition, the fraction of microtubules in the cytoplasm (in a distance of more than 7 μm from the chromosomes, green curve) is displayed. Averages and standard deviations from ten oocytes are shown.

of maturation and analyzed their microtubule organization by immunofluorescence staining 10–12 hours after enucleation. None of the enucleated oocytes formed a spindle-like structure (n = 50) but instead contained only loosely connected MTOC asters that were more clustered in cells enucleated closer to NEBD (Figure 3E). Assuming that Ran-GTP production was fully inhibited in our RanT24N experiments, the complete absence of spindle-like structures in enucleated oocytes suggests that the second phase of microtubule nucleation requires nuclear factors other than Ran.

Bivalents Individualize through Microtubule-Dependent Centrifugal Sorting

Our observation of chromosomes during MTOC centering revealed that clusters of multiple chromosomes around the nucleolus and at the nuclear envelope (Figure 4A, time −0:19), resolved into single bivalent chromosomes (Figure 4A; Movie S7). Bivalent individualization coincided with the first microtubule-chromatin contacts and MTOC aggregation (Figures 3A and 4A), indicating that these processes may be coupled. To test this, we tracked individual bivalents relative to microtubule tip dynamics (Figures 4A and 4B; Movie S7) and found that interchromosome distances increased during MTOC clustering (Figure 4E). Chromosomes that had surrounded the nucleolus individualized by centrifugal movements with a velocity of 0.54 ± 0.35 μm/min (Figures 4C and 4F) until they reached the periphery of the congressing MTOCs (Figure 4A; Movie S7). By contrast, individualization of the chromosome clusters that were already located at the periphery of the nucleus was achieved through separation on the surface of the MTOC cluster (Figure 4D) without centrifugal movement (Figure 4G). In this manner, a microtubule ball formed that carried the majority of chromosomes on its surface as single bivalents, thereby resulting in the circular bivalent configuration that has been described previously (Calarco et al., 1972). Chromosome individualization was microtubule-dependent since depolymerization of microtubules caused the collapse of chromosomes into a single chromatin mass (Figure 4H), consistent with previous observations (Longo and Chen, 1985; Van Blerkom and Bell, 1986). In summary, chromosome bivalents are individualized during MTOC clustering in a centrifugal microtubule-dependent sorting process.

Spindle Bipolarization Is Achieved by Progressive Clustering of Multiple Poles

The microtubule ball is an apolar structure formed out of many MTOCs. To analyze how it is transformed into a bipolar spindle, we recorded high-resolution 4D data of microtubule tips during spindle bipolarization (Figure 5). After MTOC aggregation was complete (Figure 5A, time 0:00–1:16), multiple poles were ejected from the microtubule ball into apparently random directions (Figure 5A, time 1:36–2:10). Immunofluorescence of γ-tubulin (Figure S7, microtubule ball) revealed well-defined γ-tubulin foci on the surface of the ball, likely corresponding to the multiple poles forming at this stage. In addition, γ-tubulin was evenly enriched inside the microtubule ball, explaining its high microtubule density. In live oocytes, these multiple poles then progressively clustered until two dominant poles had formed (Figure 5A, time 2:45–3:05) that determined the direction of bipolar spindle elongation (Figure 5A, time 3:19–3:39). At the end of spindle elongation, an acentrosomal spindle with two broad γ-tubulin-containing poles had formed (Figures 5A, time 3:39, and S7, barrel-shaped spindle).

Kinesin-5 Is Required for Pole Ejection and Spindle Bipolarization

To test whether the ejection of multiple poles and subsequent spindle elongation could be explained by activation of the tetrameric plus-end-directed motors of the kinesin-5 family, like Kif11, the mouse ortholog of Eg5 that slides antiparallel microtubules apart (Kapitein et al., 2005), we inhibited kinesin-5 activity with monastrol (Mayer et al., 1999). Even at 100 μM monastrol did not affect MTOC recruitment (Figure S8), MTOC clustering after NEBD (Figure 5B; Movie S8), or the kinetics of microtubule ball formation (1hr 10 min ± 15 min after NEBD in monastrol-treated oocytes (n = 19); 1hr 12 min ± 20 min after NEBD in DMSO-treated control oocytes (n = 11). Monastrol, however, blocked spindle assembly in the microtubule ball stage in 53/53 oocytes, while a normal spindle assembled in 44/44 DMSO-treated control oocytes (Figure 5B; Movie S8), showing that activation of kinesin-5 is required for pole ejection and bipolarization.

Astral-like Microtubules Form during Spindle Bipolarization

Once formed, the bipolar spindle surprisingly contained astral-like microtubules that probed the oocyte cortex (Figure S9; Movie S9) and may therefore participate in spindle positioning in addition to an actin-dependent process already reported in mouse oocytes (Longo and Chen, 1985). To explore the mechanism of astral-like microtubule formation, we observed individual microtubule plus ends in the process of spindle bipolarization in live oocytes (Figure 5C). During MTOC aggregation, some of the microtubule plus ends originating from the region of the forming spindle extended far into the cytoplasm

(D) The total plus-end intensity in a 7 μm radius around the chromatin was determined from oocytes expressing EB3-mEGFP and H2B-mRFP1 that were injected with RanT24N (green curve) or with an equivalent mass of BSA in identical buffer (purple curve). Both curves represent averages and standard deviations from six oocytes.

(E) Immunofluorescence of oocytes (Z-Projection: 28 slices, every 2 μm) that were enucleated at the indicated time after onset of maturation and fixed ~10–12 hr later. Microtubules are shown in green, and chromosomes are shown in red. Absence of chromatin in enucleated oocytes was confirmed by visual inspection. Scale bar is 10 μm.

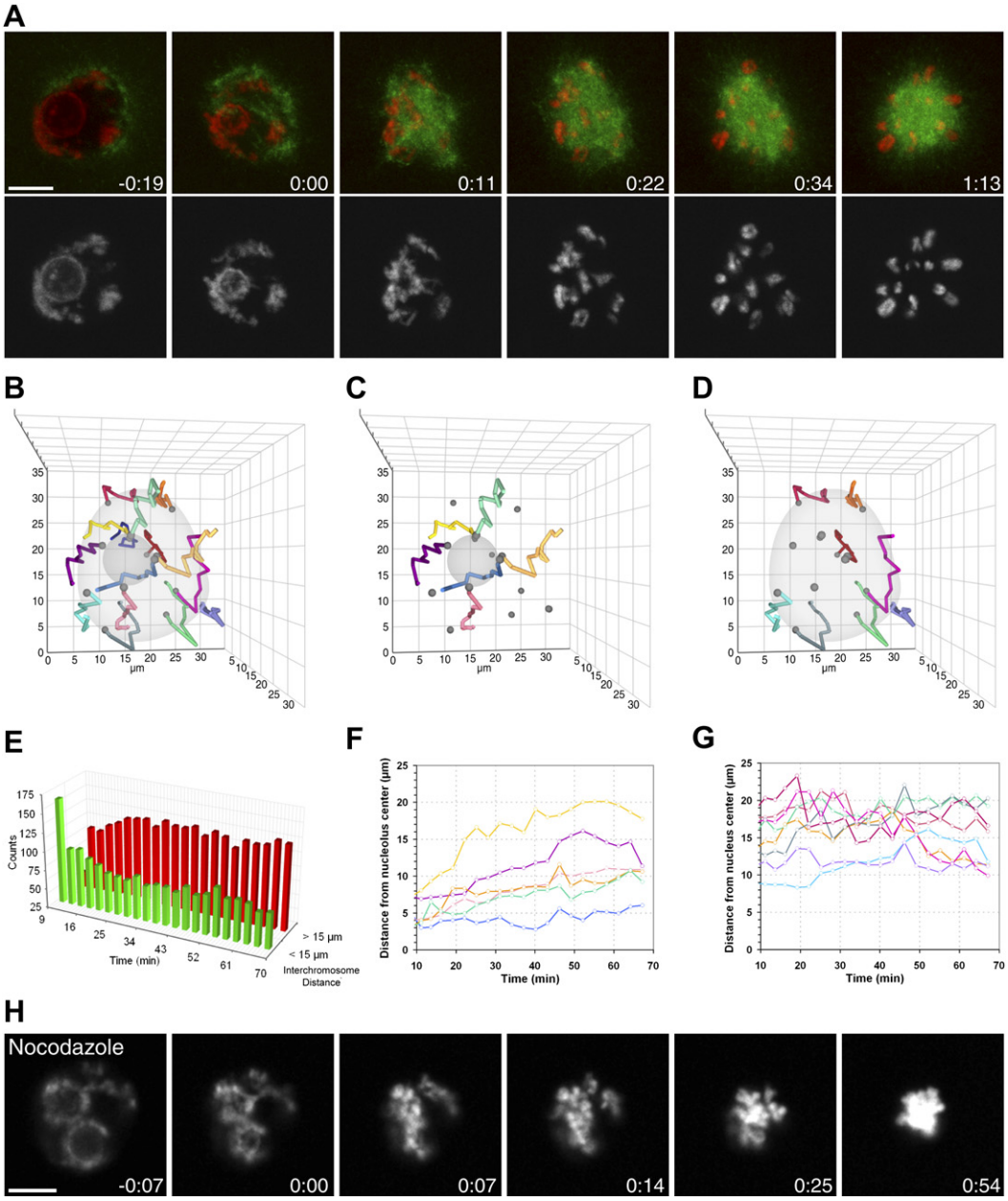

Figure 4. Bivalents Individualize through Microtubule-Dependent Centrifugal Sorting

(A) Time-lapse imaging of a maturing oocyte expressing EB3-mEGFP (microtubule plus ends, green) and H2B-mRFP1 (chromosomes, red). Z-projections (eight confocal sections, every 4 μm) of H2B-mRFP1 signal (lower panel) and merged with EB3-mEGFP signal (upper panel) are shown. Scale bar is 10 μm. Time hh:mm relative to NEBD. See also Movie S7.

(B) 3D tracks representing individual chromosome movements from 9 until 70 min after NEBD are shown. For clarity, only every second measured position is displayed as the average of two successive positions. The dark gray circle marks the region of the nucleolus; the light gray shading the nuclear envelope. Small gray spheres mark initial chromosome positions.

(C) As in (B), but only the movements of chromosomes surrounding the nucleolus are shown.

(D) As in (B), but only the movements of chromosomes in proximity to the nuclear envelope are shown.

(E) Histogram displaying the counts of interchromosome distances <15 μm (green) and >15 μm (red) from 9 until 70 min after NEBD.

(F) The distance of the nucleolus-surrounding chromosomes from the center of the nucleolus is plotted over time, relative to NEBD. The colors of the curves correspond to the colors of the respective chromosome tracks shown in (C).

(G) The distance of the chromosomes in proximity to the nuclear envelope is plotted over time, relative to NEBD. The colors of the curves correspond to the colors of the respective chromosome tracks shown in (D).

(H) Time-lapse imaging of an oocyte maturing in the presence of 3 μg/ml nocodazole. The oocyte expresses H2B-mRFP1 (chromosomes). Tracking the chromosomes was not possible due to the lack of chromosome individualization. Scale bar is 10 μm. Time hh:mm relative to NEBD.

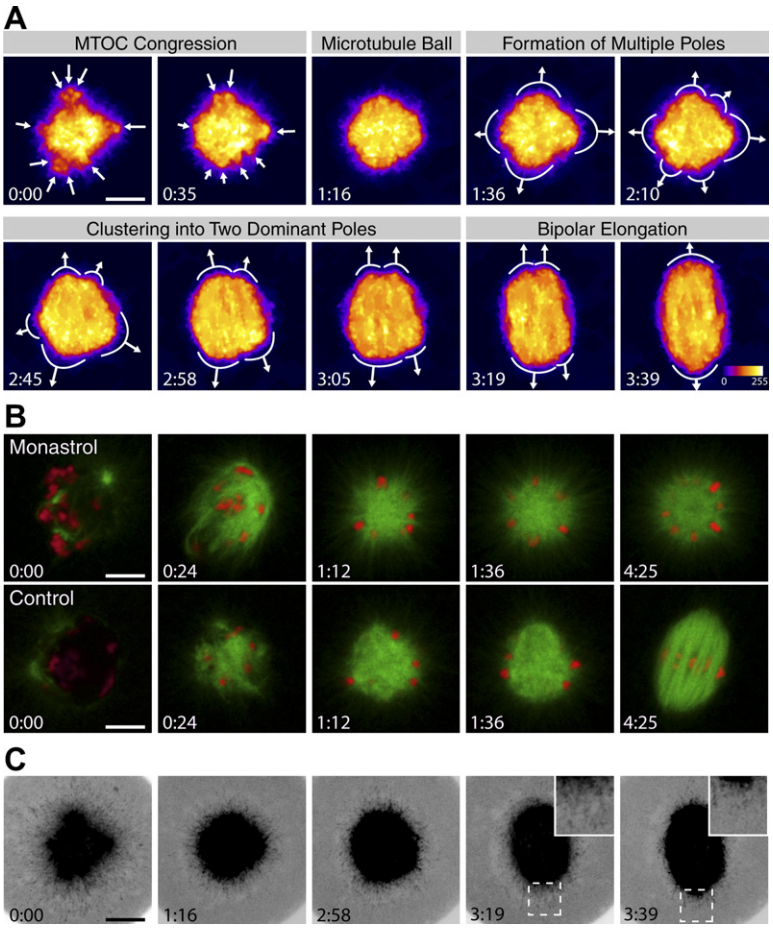

Figure 5. Kinesin-5-Dependent Spindle Bipolarization and Astral Microtubule Formation

(A) Time-lapse imaging of a maturing oocyte expressing EB3-mEGFP (microtubule plus ends). Z-projections of two anisotropic diffusion-filtered optical sections, 6 μm apart, are represented in pseudocolor. The corresponding look-up table is shown as a bar (last panel). White arrows mark the directionality of MTOC movements and highlight pole positions. Scale bar is 10 μm. Time, hh:mm.

(B) Time-lapse imaging of maturing oocytes expressing EGFP-MAP4 (microtubules, green) and H2B-mRFP1 (chromosomes, red) that were treated with 100 μM monastrol (upper panel) or DMSO (lower panel). Scale bar is 10 μm. Time hh:mm. See also Movie S8.

(C) Time-lapse imaging of a maturing oocyte expressing EB3-mEGFP. Z-projections of two contrast and brightness adjusted and inverted optical sections, 6 μm apart, are shown. At time 3:19 and 3:39, insets show magnified astral-like microtubule plus ends. Scale bar is 10 μm. Time, hh:mm. See also Movie S9.

(Figure 5C, time 0:00; Movie S5). The length of these microtubules decreased while the microtubule ball formed, but a significant number of plus ends remained orientated toward the cytoplasm (Figure 5C, time 0:00–1:16). During bipolarization, the plus ends of outer microtubules located between the two poles became integrated into the spindle body, while the length of microtubules pointing from the poles to the cortex increased, thereby producing astral-like microtubules (Figure 5C, time 2:58–3:39).

Spindle Bipolarization Precedes Chromosome Biorientation

The axis of the bipolarizing spindle could be determined by MTOC self-organization or the chromosome configuration. To discriminate between these possibilities, we analyzed whether chromosome biorientation precedes spindle elongation (Figures 6B and 6E) by measuring the fraction of bioriented chromosomes and the increase in spindle length over time (for details, see Supplemental Experimental Procedures). We found that individual chromosome bivalents were bioriented during spindle elongation in an ~30 min stretching process with linear kinetics (Figures 6A and 6D) only after spindle elongation was initiated (Figures 6B and 6E). Thus, spindle bipolarization is independent of chromosome biorientation and therefore most likely achieved through motor-mediated MTOC self-organization.

Bioriented Chromosomes Oscillate around the Metaphase Plate

To test if the acentrosomal metaphase I spindle exhibits additional functional characteristics of centrosomal spindles, we analyzed the dynamic behavior of bioriented chromosomes by tracking their position relative to the spindle midplane over time (Figure 6C). We found that after initial biorientation, the majority of chromosomes did not revert to monopolar attachment. Interestingly, stable chromosome biorientation not only occurred without detectable kinetochore fibers, but, at a time, when microtubule bundles were conspicuously absent from the ends of the telocentric bivalent chromosomes (Figure 6C, time 1:10, arrow). Once bioriented, the chromosomes performed slow oscillatory movements with a range of up to 3 μm around the metaphase plate (Figure 6F) reaching maximum velocities of ~0.5 μm/min, with average velocities around only 0.1 ± 0.1μm/min. This is in contrast to chromosome behavior in *Xenopus* egg extract spindles, where chromosomes do not oscillate (Desai et al., 1998; Maddox et al., 2003). However, the oscillatory chromosome velocities we measured were lower than those

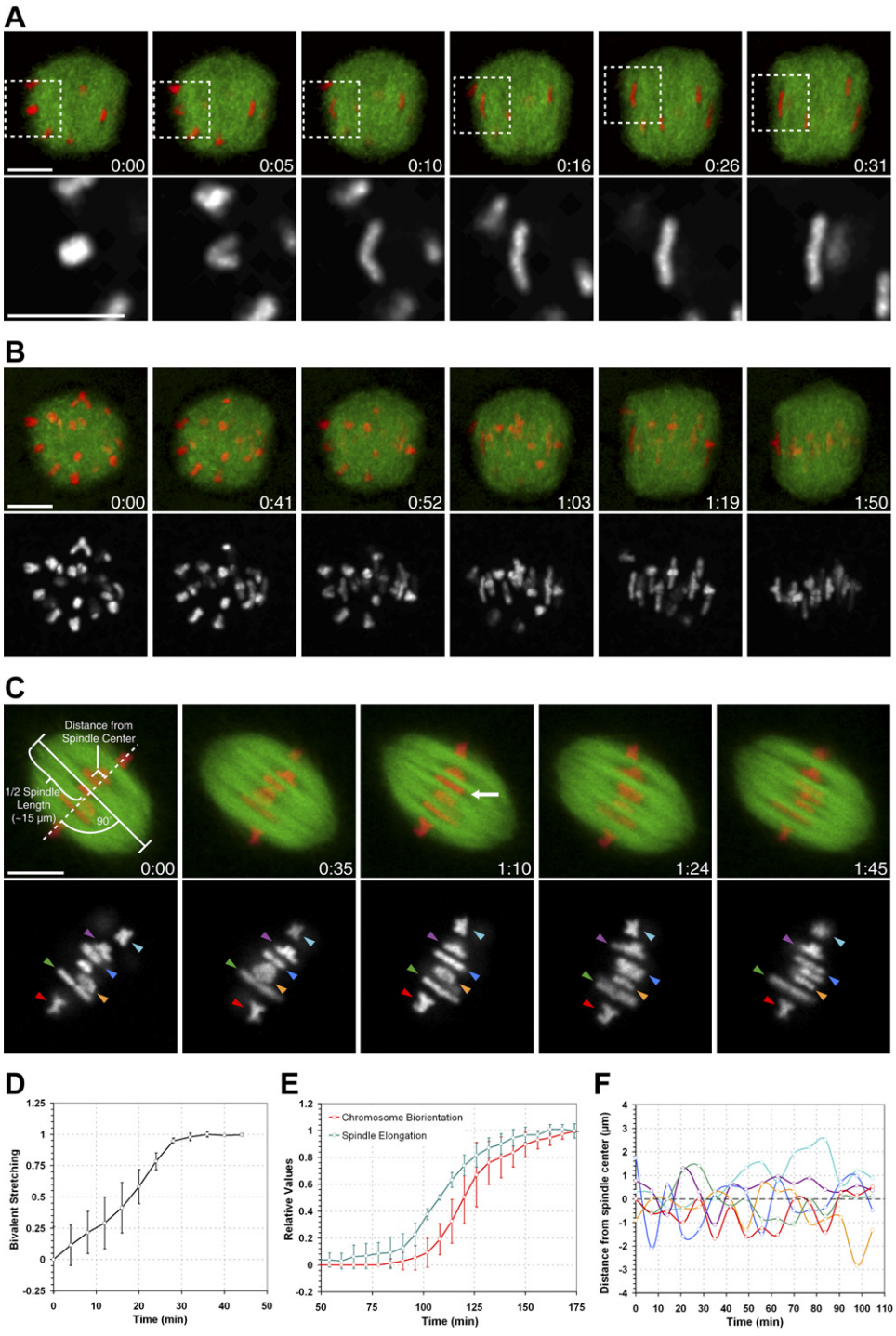

Figure 6. Spindle Elongation Precedes Chromosome Biorientation

(A) Time-lapse imaging of a maturing oocyte expressing EB3-mEGFP (microtubule plus ends, green) and H2B-mRFP1 (chromosomes, red; upper panel). Boxed regions are magnified for the H2B-mRFP1 signal only in the lower panel. Scale bar is 10 μm. Time, hh:mm.

(B) Time-lapse imaging of a maturing oocyte expressing EB3-mEGFP (microtubule plus ends, green) and H2B-mRFP1 (chromosomes, red). Z-projections (five confocal sections, every 5 μm) of H2B-mRFP1 signal (lower panel) and merged with EB3-mEGFP signal (upper panel) are shown. Scale bar is 10 μm. Time, hh:mm.

(C) Time-lapse imaging of a maturing oocyte expressing EGFP-MAP4 (microtubules, green) and H2B-mRFP1 (chromosomes, red), merged (upper panel), or H2B-mRFP1 only (lower panel). Relative chromosome positions are marked by colored arrowheads. White arrow (Time: 1:10) highlights the absence of microtubule bundles at kinetochores. Scale bar is 10 μm. Time, hh:mm.

reported for mitotic systems (~1.7 μm/min; Skibbens et al., 1993).

DISCUSSION

Eighty MTOCs Are Formed De Novo and Participate in Spindle Assembly

Our study clarifies several controversial issues in literature regarding the origin and number of MTOCs that participate in spindle assembly in mouse oocytes. First, we found that, on average, more than 80 MTOCs of variable sizes are present in oocytes before NEBD. Previous studies reported fewer than 14 MTOCs (Messinger and Albertini, 1991; Van Blerkom, 1991) but are likely to have missed smaller MTOCs due to resolution limitations of wide-field fluorescence microscopy in thick oocytes. Second, our data clearly show that spindle assembly involves both perinuclear as well as cytoplasmic MTOCs, a controversial issue in previous reports (Calarco, 2000; Combelles and Albertini, 2001; Messinger and Albertini, 1991; Van Blerkom, 1991). Third, we could demonstrate that the vast majority of MTOCs are formed de novo from the interphase-like microtubule network that spans the cytoplasm of the oocyte during early prophase arrest. This is consistent with a previous report (Mattson and Albertini, 1990) but does not support the model that MTOCs form during meiotic maturation (Calarco, 2000) by disintegration of a large γ-tubulin-positive "multivesicular aggregate."

A New Comprehensive Model for Acentrosomal Spindle Assembly

This study is the first analysis of meiotic spindle assembly in live mammalian oocytes using high-resolution confocal microscopy. Our quantitative analysis of single chromosome, MTOC, and microtubule plus-end behavior combined with targeted inhibition experiments (summarized in Figure 7A) enables us to propose a new model of in vivo acentrosomal spindle assembly based on self-organization of multiple MTOCs by sequential activation of three different microtubule motor activities (Figure 7B).

Our data reveal that after their de novo formation, MTOCs moved centripetally by attracting each other through direct MTOC-MTOC contacts, in agreement with previous electron microscopy observations (Van Blerkom, 1991), and by direct interactions with the nuclear envelope (Figure 7B, panel I). The attracting forces between MTOCs and MTOCs and the nuclear envelope are consistent with the action of oligomeric minus-end-directed motor proteins (Figure 7B, panel I), such as dynein or members of the kinesin-14 family, like Ncd, which are known to act at the nuclear envelope of mammalian cells (Beaudouin et al., 2002; Salina et al., 2002) and at microtubule asters in *Drosophila* oocytes (Skold et al., 2005). Dynein also drives the inward motion of microtubule bundles at the G2-M transition in mitotic cells (Rusan et al., 2002), reminiscent of MTOC recruitment in mouse oocytes.

MTOCs remained the predominant nucleation sites of new microtubule plus ends as long as they could be spatially distinguished from chromosomes. Immediately after NEBD, MTOCs mediated a RanGTP-dependent enormous increase in microtubule mass, consistent with Ran's requirement to activate several spindle assembly factors (Goodman and Zheng, 2006). After a 2 hr delay, the number of microtubules slowly increased to about half the normal number in oocytes, where Ran-GTP production was inhibited. This increase was sufficient for the delayed formation of a smaller bipolar spindle. In enucleated oocytes, bipolar spindles were absent, suggesting that nuclear factors other than Ran support the delayed and weak spindle formation when Ran-GTP production is inhibited. Our data are consistent with a recent report that suggested that the assembly of the metaphase I spindle in mouse and *Xenopus* oocytes is Ran independent (Dumont et al., 2007) and provides the explanation why spindles formed in the absence of Ran-GTP are delayed and smaller than normal. It will be necessary to investigate whether Ran-independent spindles support segregation of bivalents and polar body extrusion with the same fidelity as normal spindles before concluding that Ran is dispensable for spindle function in meiosis I.

After MTOC centering and the increase in microtubule number, spindle assembly proceeded by centrifugal sorting of chromosome clusters into single bivalents on the surface of a microtubule ball, resulting in the circular bivalent configuration (Calarco et al., 1972; Figure 7B, panels I–III). Centrifugal chromosome movements during individualization are likely driven by interactions of microtubules with chromosome arms since kinetochores were randomly orientated relative to microtubules (Figure 7B, panel III). The velocities of ~0.53 μm/min of chromosomes toward the plus ends of microtubules are consistent with the action of chromokinesins, plus-end-directed motors with low processivity known to be involved in chromosome alignment on the surface of monoasters (Antonio et al., 2000; Levesque and Compton, 2001; Yajima et al., 2003).

Next, the microtubule ball (Figure 7B, panel III) was transformed into a bipolar spindle through a series of MTOC clustering events (Figure 7B, panels IV–VI). First, MTOCs formed multiple spindle poles that were ejected from the microtubule ball (Figure 7B, panel IV). We found

(D) Quantitative analysis of individual bivalent stretching as shown in (A). The normalized angle between the two bivalent arms is plotted over time. Averages and standard deviations from 12 measurements are shown.

(E) Quantitative analysis of spindle elongation and total chromosome biorientation as shown in (B). The normalized spindle elongation (green curve) and the fraction of bioriented chromosomes (red curve) are plotted over time. Averages and standard deviations from five independent experiments are shown.

(F) Quantitative analysis of chromosome oscillations around the metaphase plate as shown in (C). The distance of the chromosome centers from the spindle center is plotted over time. Determination of metaphase plate and chromosome positions were performed as illustrated in (C; 0:00). The colors of the curves correspond to the arrowhead colors marking the different chromosomes in (C).

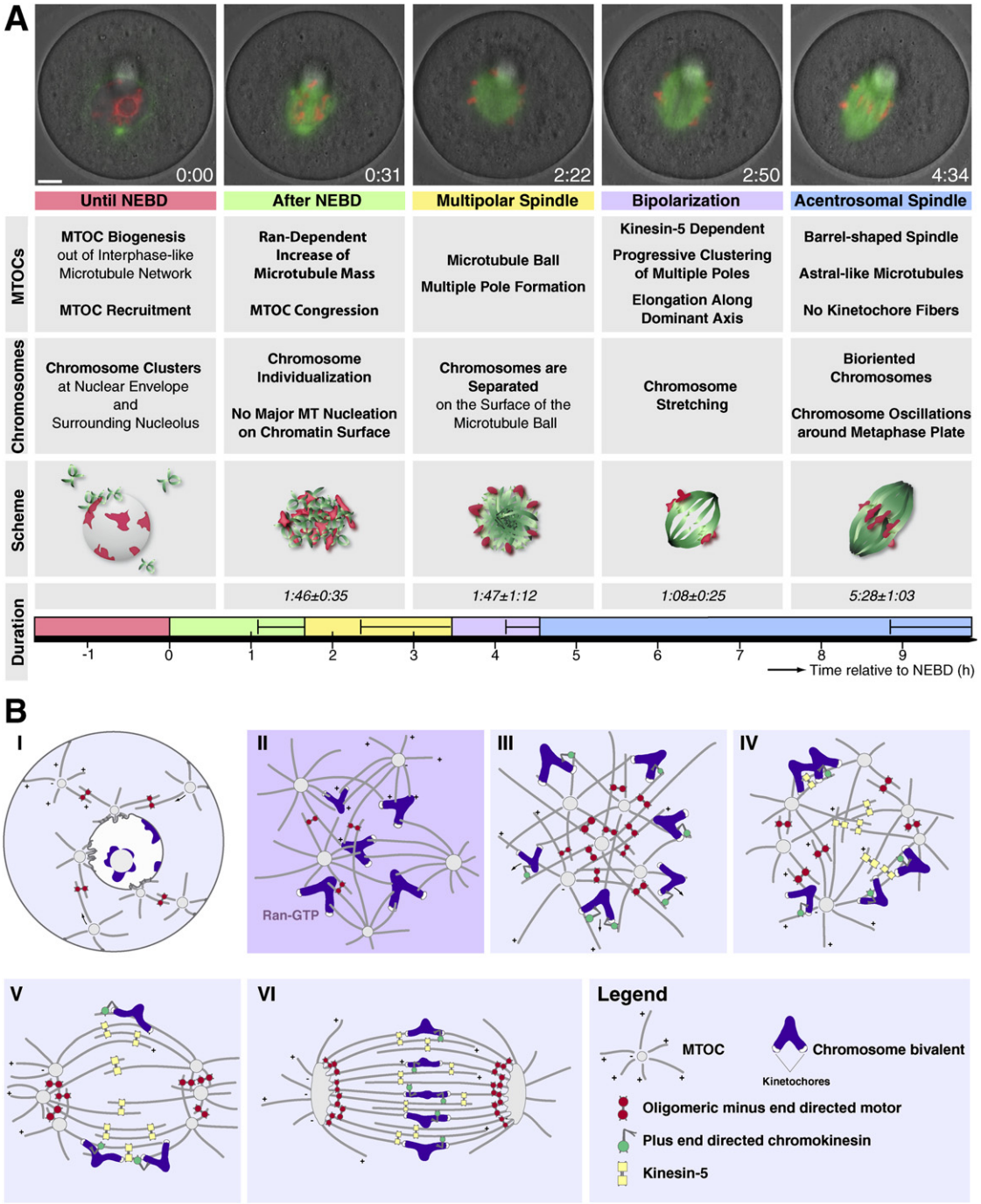

Figure 7. A New Model of Acentrosomal Spindle Assembly

(A) Summary of acentrosomal spindle assembly in mouse oocytes. The different stages of spindle assembly (color-labeled fields), their duration (duration; colored bars refer to color-labeled fields; averages and standard deviations from 14 experiments are shown), a schematic representation of each stage (scheme), as well as the corresponding MTOC (MTOCs)- and chromosome (chromosomes)-related events are listed. The top panel shows stage-specific time-lapse images of a maturing oocyte expressing EGFP-MAP4 (microtubules, green) and H2B-mRFP1 (chromosomes, red) merged with DIC. The sphere in the cytoplasm visible in the DIC channel is an oil droplet resulting from the microinjection procedure. Scale bar is 10 μm. Time, hh:mm relative to NEBD. See also Movie S10.

(B) Mechanistic model of acentrosomal spindle assembly in mouse oocytes. The different objects are specified in the legend field. Arrows describe directionality of MTOC (I) or chromosome (III) movement, respectively. For details, see Discussion.

that Kif11 (kinesin-5), the mouse ortholog of Eg5, is required for multiple pole ejection and spindle bipolarization (Figure 7B, panel IV). The continued activity of oligomeric minus-end-directed motors such as dynein or Ncd that led to the initial MTOC centering would counteract Kif11 and promote MTOC clustering, explaining the fusion of several small poles into larger ones until two dominant spindle poles had formed (Figure 7B, panel V). Only in this bipolar configuration can microtubules be stably aligned by the two opposed motor activities (Karsenti and Nedelec, 2004).

Once a bipolar spindle axis had been established, the spindle elongated, presumably also driven by kinesin-5 (Figure 7B, panel VI). Spindle elongation was followed by the establishment of chromosome biorientation, indicating that microtubule kinetochore contacts had formed. However, we did not observe prominent fibers ending at telocentric kinetochores throughout metaphase I, which may explain why kinetochore microtubule interactions could not be detected in an ultrastructural study in this stage (Brunet et al., 1999). In addition, chromokinesins are likely to link chromosomes to microtubules and thereby support chromosome alignment (Figure 7B, panel VI). In total, metaphase I spindle assembly takes more than 4 hr (Figure 7A). In contrast, the metaphase II spindle forms within only ~90 min by reorganization of the half of the central spindle that stays in the oocyte after polar body extrusion (data not shown).

In summary, a simple model of sequential activation of three known microtubule motor activities and a Ran-dependent increase of the number of microtubules after NEBD are sufficient to explain the apparently complex series of MTOC self-organization intermediates we observed during spindle formation in meiosis I of mouse oocytes. This mechanism produced a bipolar acentrosomal spindle that shares most properties of centrosomal mitotic spindles, including astral-like microtubules and oscillating chromosomes. In contrast to centrosome containing prepolarized starfish oocytes (Lenart et al., 2005), filamentous actin was not required for correct chromosome capture and spindle assembly (Figure S10), as was also reported previously (Wassarman and Fujiwara, 1978). In addition to kinesin-5, our model proposes clear candidate microtubule motor activities that will be very interesting to test in future studies using the live cell imaging assays we established. Female germline-specific mouse knockout approaches (Kudo et al., 2006) will be invaluable for such studies as many of the involved activities are likely to be essential for embryonic development. Finally, it is interesting to note that the reverse process occurs before fertilization, when MTOCs transform into a fine microtubule lattice filling the mouse egg during pronuclear migration (Schatten et al., 1985). Thus, the de novo formation and disassembly of numerous MTOCs apparently serve as a flexible microtubule organizing system for several essential microtubule-dependent steps of meiosis and fertilization in mammalian oocytes.

EXPERIMENTAL PROCEDURES

Preparation and Culture of Oocytes

Ovaries were collected from 8-week-old FVB or 3-week-old SJLxB6 F1 mice that were maintained according to the guidelines of EMBL Laboratory Animal Resources, 44–48 hr after priming with 5 IU pregnant mare serum gonadotropin. Oocytes were isolated by puncturing the ovaries with needles in M2 medium. If oocytes were isolated for microinjection, the medium was supplemented with 250 μM dbcAMP (dibutyryl cyclic AMP) to maintain prophase arrest. For immunofluorescence analysis in Figures 1A, 2D, S5, S7, S9, and S10A freshly isolated oocytes without dbcAMP arrest were used. Residual follicle cells were removed by mouth pipetting. To induce resumption of meiosis, oocytes were washed with and incubated in dbcAMP free medium. For live cell imaging, oocytes were cultured in LabTek chambered cover glasses (Nunc) in either M2 medium maintained at 37°C by an air stream incubator (ASI 400; Nevtek) and an objective heater (Bioptechs) or in M16 medium in an EMBL environmental microscope incubator (EMBL, GP 106) allowing cells to be maintained in a 5% CO_2 atmosphere at 37°C with humidity control during imaging. To improve the adhesiveness of the oocytes, the zona pellucida was partially removed in some experiments using Tyrode's acidic solution (Sigma). Under these culture conditions, the efficiency of polar body extrusion was 82 ± 9%; only 13 ± 4% of the oocytes arrested in metaphase I and only 5 ± 6% died, mostly at the beginning of the experiment, due to rupture of the plasma membrane by Tyrode's acidic solution (five independent experiments, 63 oocytes). In some experiments, the medium was supplemented with 3 μg/ml nocodazole, 3 μg/ml cytochalasin D, 100 μM monastrol (Sigma), or corresponding amounts of DMSO in controls.

Micromanipulation

Oocytes were injected based on methods described elsewhere (Jaffe and Terasaki, 2004) with some modifications. To hold the oocytes during microinjection, an "injection slit" was generated by assembling two coverslips around a spacer consisting of a 100 μm thick piece of double stick tape. The oocytes were strung in the slit by mouth pipetting and pushed to the base of the slit using the injection needle so that the resistance of the adjacent tape kept the oocytes in place during the microinjection procedure. The injected volumes ranged between 10–15 pl (3%–5% of the oocyte volume) of 1–2 μg/μl mRNA. The concentration of RanT24N (Franz et al., 2007) after microinjection (15 pl of 268 μM stock) was 13 μM, corresponding to an ~4–13-fold excess over endogenous Ran in *Xenopus* eggs (Clarke and Zhang, 2001; Palacios et al., 1996). After injection, the oocytes were collected from the slit by suction applied with a mouth pipette. mRNA-injected oocytes were incubated at 37°C for 2–3 hr in M2 medium containing dbcAMP as described above to allow recombinant protein expression.

Enucleation was based on methods described previously (McGrath and Solter, 1983). Briefly, oocytes were incubated in medium containing 3 μg/ml cytochalasin D for 30 mins before removal of the karyoplast using Eppendorf TransferTips (ES).

Confocal Microscopy and Image Analysis

Time-lapse image acquisitions were performed using a customized Zeiss LSM510 confocal microscope equipped with a 40× C-Apochromat 1.2 NA water immersion objective lens (Carl Zeiss, Jena) with an in-house-developed 3D multilocation tracking macro (Rabut and Ellenberg, 2004). Typically, we recorded the whole oocyte volume or a subvolume centered around chromosomes by 3D time-lapse (4D) imaging for multiple cells in parallel.

GFP was excited with the 488 nm line of an argon laser and detected by using a 505–550 nm band-pass or a 500 nm long-pass emission filter. mRFP1 was either excited using a 532 nm solid-state laser and detected with a 545 nm long-pass emission filter or with a 543 nm helium/neon laser in combination with a 560 nm long-pass emission filter.

3D reconstructions and tracking were performed using Imaris (Bitplane). Microtubule growth rates were determined with an in-house-developed kymograph macro (http://www.embl.de/eamnet/html/kymograph.html) in ImageJ (http://rsb.info.nih.gov/ij/). Growth rates and tracks were analyzed with Excel (Microsoft). Figures were assembled with Illustrator and Photoshop (Adobe Systems).

Expression Constructs and mRNA Synthesis

To generate the constructs for in vitro RNA synthesis, the EGFP (Clontech) or mRFP1 (Campbell et al., 2002) coding sequence and previously published protein-coding sequences were fused to obtain H2B-mRFP1 (Kanda et al., 1998), EGFP-MAP4 (Olson and Olmsted, 1999), EB3-mEGFP (Stepanova et al., 2003), and C-moesin-mRFP1 (Litman et al., 2000) and were inserted into pGEMHE (Liman et al., 1992) for in vitro transcription. After linearization of the template with AscI, capped mRNA was synthesized using T7 polymerase (mMessage mMachine kit, following manufacturer's instructions, Ambion) and dissolved in 11 μl water. mRNA concentrations were determined on ethidium bromide agarose gels by comparison with an RNA standard (Ambion).

Immunofluorescence

For optimal preservation of cytoskeletal oocyte structures, all-in-one microdishes suitable for fixation, immunofluorescence staining, and subsequent microscopy were assembled. To generate the microdishes, holes (Ø 6 mm) were punched into an ~1 mm thick silicone mat (EMBL, mechanical workshop), which was then assembled on a 1-well LabTek chambered cover glass (Nunc) using silicone grease (Bayer). All steps described below were performed in the microdishes by exchanging the supernatant liquid while the oocytes resided at the bottom of the dish. After removal of the zona pellucida using Tyrode's acidic solution, oocytes were fixed for 1 hr at 37°C with 100 mM HEPES, 50 mM EGTA, 10 mM $MgSO_4$, 2% Formaldehyde, and 0.2% Triton X-100 and extracted in PBS supplemented with 0.1% Triton X-100 at 4°C overnight based on methods described elsewhere (Strickland et al., 2004). Antibody incubations were performed in PBS, 3% BSA, and 0.1% Triton X-100 using mouse anti-α-tubulin (DM 1A, Sigma; 1:700), anti-γ-tubulin (GTU 88, Sigma; 1:250), anti-pericentrin (30, BD Biosciences; 1:300), and rat anti-tyrosinated-α-tubulin (YL1/2, Serotec; 1:100) as primary antibodies and Alexa-488-labeled anti-mouse (Molecular Probes; 1:500) or Alexa-680-labeled anti-rat (Molecular Probes; 1:200) as secondary antibodies at 25°C for 2 hr. Actin was stained with rhodamine-phalloidin (Molecular Probes; 1:100). DNA was stained with 5 μg/ml Hoechst 33342 (Molecular Probes).

Supplemental Data

Supplemental Data include Experimental Procedures, References, ten figures, and ten movies and can be found with this article online at http://www.cell.com/cgi/content/full/130/3/484/DC1/.

ACKNOWLEDGMENTS

We thank Laurinda Jaffe for instructions in mouse oocyte handling; Nathalie Daigle for technical advice and for pGEMHE-EGFP-MAP4 DNA construct; Lucia Sironi for pGEMHE-EB3-mEGFP DNA construct; the staff of EMBL Laboratory Animal Resources for expert technical assistance; Péter Lénárt, Mark Terasaki, and the members of the Ellenberg lab for helpful discussions; Rudolf Walczak and Iain Mattaj for RanT24N protein; Takashi Hiiragi for anti-pericentrin antibody; and Kim Nasmyth and Martin Anger for anti-tyrosinated-α-tubulin antibody. M.S. was supported by a predoctoral fellowship through the EMBL International PhD Programme.

Received: November 10, 2006
Revised: March 23, 2007
Accepted: June 13, 2007
Published: August 9, 2007

REFERENCES

Antonio, C., Ferby, I., Wilhelm, H., Jones, M., Karsenti, E., Nebreda, A.R., and Vernos, I. (2000). Xkid, a chromokinesin required for chromosome alignment on the metaphase plate. Cell *102*, 425–435.

Bastiaens, P., Caudron, M., Niethammer, P., and Karsenti, E. (2006). Gradients in the self-organization of the mitotic spindle. Trends Cell Biol *16*, 125–134.

Beaudouin, J., Gerlich, D., Daigle, N., Eils, R., and Ellenberg, J. (2002). Nuclear envelope breakdown proceeds by microtubule-induced tearing of the lamina. Cell *108*, 83–96.

Belmont, L.D., Hyman, A.A., Sawin, K.E., and Mitchison, T.J. (1990). Real-time visualization of cell cycle-dependent changes in microtubule dynamics in cytoplasmic extracts. Cell *62*, 579–589.

Brunet, S., and Maro, B. (2005). Cytoskeleton and cell cycle control during meiotic maturation of the mouse oocyte: integrating time and space. Reproduction *130*, 801–811.

Brunet, S., Maria, A.S., Guillaud, P., Dujardin, D., Kubiak, J.Z., and Maro, B. (1999). Kinetochore fibers are not involved in the formation of the first meiotic spindle in mouse oocytes, but control the exit from the first meiotic M phase. J. Cell Biol. *146*, 1–12.

Calarco, P.G. (2000). Centrosome precursors in the acentriolar mouse oocyte. Microsc. Res. Tech. *49*, 428–434.

Calarco, P.G., Donahue, R.P., and Szollosi, D. (1972). Germinal vesicle breakdown in the mouse oocyte. J. Cell Sci. *10*, 369–385.

Campbell, R.E., Tour, O., Palmer, A.E., Steinbach, P.A., Baird, G.S., Zacharias, D.A., and Tsien, R.Y. (2002). A monomeric red fluorescent protein. Proc. Natl. Acad. Sci. USA *99*, 7877–7882.

Can, A., Semiz, O., and Cinar, O. (2003). Centrosome and microtubule dynamics during early stages of meiosis in mouse oocytes. Mol. Hum. Reprod. *9*, 749–756.

Carabatsos, M.J., Combelles, C.M., Messinger, S.M., and Albertini, D.F. (2000). Sorting and reorganization of centrosomes during oocyte maturation in the mouse. Microsc. Res. Tech. *49*, 435–444.

Caudron, M., Bunt, G., Bastiaens, P., and Karsenti, E. (2005). Spatial coordination of spindle assembly by chromosome-mediated signaling gradients. Science *309*, 1373–1376.

Clarke, P.R., and Zhang, C. (2001). Ran GTPase: a master regulator of nuclear structure and function during the eukaryotic cell division cycle? Trends Cell Biol. *11*, 366–371.

Combelles, C.M., and Albertini, D.F. (2001). Microtubule patterning during meiotic maturation in mouse oocytes is determined by cell cycle-specific sorting and redistribution of gamma-tubulin. Dev. Biol. *239*, 281–294.

Desai, A., Maddox, P.S., Mitchison, T.J., and Salmon, E.D. (1998). Anaphase A chromosome movement and poleward spindle microtubule flux occur At similar rates in Xenopus extract spindles. J. Cell Biol. *141*, 703–713.

Dumont, J., Petri, S., Pellegrin, F., Terret, M.E., Bohnsack, M.T., Rassinier, P., Georget, V., Kalab, P., Gruss, O.J., and Verlhac, M.H. (2007). A centriole- and RanGTP-independent spindle assembly pathway in meiosis I of vertebrate oocytes. J. Cell Biol. *176*, 295–305.

Franz, C., Walczak, R., Yavuz, S., Santarella, R., Gentzel, M., Askjaer, P., Galy, V., Hetzer, M., Mattaj, I.W., and Antonin, W. (2007). MEL-28/ELYS is required for the recruitment of nucleoporins to chromatin and postmitotic nuclear pore complex assembly. EMBO Rep. *8*, 165–172.

Gard, D.L. (1992). Microtubule organization during maturation of Xenopus oocytes: assembly and rotation of the meiotic spindles. Dev. Biol. *151*, 516–530.

Goodman, B., and Zheng, Y. (2006). Mitotic spindle morphogenesis: Ran on the microtubule cytoskeleton and beyond. Biochem. Soc. Trans. *34*, 716–721.

Gueth-Hallonet, C., Antony, C., Aghion, J., Santa-Maria, A., Lajoie-Mazenc, I., Wright, M., and Maro, B. (1993). gamma-Tubulin is present in acentriolar MTOCs during early mouse development. J. Cell Sci. *105*, 157–166.

Hayden, J.H., Bowser, S.S., and Rieder, C.L. (1990). Kinetochores capture astral microtubules during chromosome attachment to the mitotic spindle: direct visualization in live newt lung cells. J. Cell Biol. *111*, 1039–1045.

Heald, R., Tournebize, R., Blank, T., Sandaltzopoulos, R., Becker, P., Hyman, A., and Karsenti, E. (1996). Self-organization of microtubules into bipolar spindles around artificial chromosomes in Xenopus egg extracts. Nature *382*, 420–425.

Jaffe, L.A., and Terasaki, M. (2004). Quantitative microinjection of oocytes, eggs, and embryos. Methods Cell Biol. *74*, 219–242.

Kalab, P., Pralle, A., Isacoff, E.Y., Heald, R., and Weis, K. (2006). Analysis of a RanGTP-regulated gradient in mitotic somatic cells. Nature *440*, 697–701.

Kanda, T., Sullivan, K.F., and Wahl, G.M. (1998). Histone-GFP fusion protein enables sensitive analysis of chromosome dynamics in living mammalian cells. Curr. Biol. *8*, 377–385.

Kapitein, L.C., Peterman, E.J., Kwok, B.H., Kim, J.H., Kapoor, T.M., and Schmidt, C.F. (2005). The bipolar mitotic kinesin Eg5 moves on both microtubules that it crosslinks. Nature *435*, 114–118.

Karsenti, E., and Nedelec, F. (2004). The mitotic spindle and actin tails. Biol. Cell *96*, 237–240.

Klebe, C., Bischoff, F.R., Ponstingl, H., and Wittinghofer, A. (1995). Interaction of the nuclear GTP-binding protein Ran with its regulatory proteins RCC1 and RanGAP1. Biochemistry *34*, 639–647.

Kudo, N.R., Wassmann, K., Anger, M., Schuh, M., Wirth, K.G., Xu, H., Helmhart, W., Kudo, H., McKay, M., Maro, B., et al. (2006). Resolution of chiasmata in oocytes requires separase-mediated proteolysis. Cell *126*, 135–146.

Lenart, P., Bacher, C.P., Daigle, N., Hand, A.R., Eils, R., Terasaki, M., and Ellenberg, J. (2005). A contractile nuclear actin network drives chromosome congression in oocytes. Nature *436*, 812–818.

Levesque, A.A., and Compton, D.A. (2001). The chromokinesin Kid is necessary for chromosome arm orientation and oscillation, but not congression, on mitotic spindles. J. Cell Biol. *154*, 1135–1146.

Liman, E.R., Tytgat, J., and Hess, P. (1992). Subunit stoichiometry of a mammalian K+ channel determined by construction of multimeric cDNAs. Neuron *9*, 861–871.

Litman, P., Amieva, M.R., and Furthmayr, H. (2000). Imaging of dynamic changes of the actin cytoskeleton in microextensions of live NIH3T3 cells with a GFP fusion of the F-actin binding domain of moesin. BMC Cell Biol. *1*, 1.

Longo, F.J., and Chen, D.Y. (1985). Development of cortical polarity in mouse eggs: involvement of the meiotic apparatus. Dev. Biol. *107*, 382–394.

Maddox, P., Straight, A., Coughlin, P., Mitchison, T.J., and Salmon, E.D. (2003). Direct observation of microtubule dynamics at kinetochores in Xenopus extract spindles: implications for spindle mechanics. J. Cell Biol. *162*, 377–382.

Manandhar, G., Schatten, H., and Sutovsky, P. (2005). Centrosome reduction during gametogenesis and its significance. Biol. Reprod. *72*, 2–13.

Maro, B., Howlett, S.K., and Webb, M. (1985). Non-spindle microtubule organizing centers in metaphase II-arrested mouse oocytes. J. Cell Biol. *101*, 1665–1672.

Mattson, B.A., and Albertini, D.F. (1990). Oogenesis: chromatin and microtubule dynamics during meiotic prophase. Mol. Reprod. Dev. *25*, 374–383.

Mayer, T.U., Kapoor, T.M., Haggarty, S.J., King, R.W., Schreiber, S.L., and Mitchison, T.J. (1999). Small molecule inhibitor of mitotic spindle bipolarity identified in a phenotype-based screen. Science *286*, 971–974.

McGrath, J., and Solter, D. (1983). Nuclear transplantation in the mouse embryo by microsurgery and cell fusion. Science *220*, 1300–1302.

Messinger, S.M., and Albertini, D.F. (1991). Centrosome and microtubule dynamics during meiotic progression in the mouse oocyte. J. Cell Sci. *100*, 289–298.

Olson, K.R., and Olmsted, J.B. (1999). Analysis of microtubule organization and dynamics in living cells using green fluorescent protein-microtubule-associated protein 4 chimeras. Methods Enzymol. *302*, 103–120.

Palacios, M.J., Joshi, H.C., Simerly, C., and Schatten, G. (1993). Gamma-tubulin reorganization during mouse fertilization and early development. J. Cell Sci. *104*, 383–389.

Palacios, I., Weis, K., Klebe, C., Mattaj, I.W., and Dingwall, C. (1996). RAN/TC4 mutants identify a common requirement for snRNP and protein import into the nucleus. J. Cell Biol. *133*, 485–494.

Piehl, M., Tulu, U.S., Wadsworth, P., and Cassimeris, L. (2004). Centrosome maturation: measurement of microtubule nucleation throughout the cell cycle by using GFP-tagged EB1. Proc. Natl. Acad. Sci. USA *101*, 1584–1588.

Rabut, G., and Ellenberg, J. (2004). Automatic real-time three-dimensional cell tracking by fluorescence microscopy. J. Microsc. *216*, 131–137.

Rusan, N.M., Fagerstrom, C.J., Yvon, A.M., and Wadsworth, P. (2001). Cell cycle-dependent changes in microtubule dynamics in living cells expressing green fluorescent protein-alpha tubulin. Mol. Biol. Cell *12*, 971–980.

Rusan, N.M., Tulu, U.S., Fagerstrom, C., and Wadsworth, P. (2002). Reorganization of the microtubule array in prophase/prometaphase requires cytoplasmic dynein-dependent microtubule transport. J. Cell Biol. *158*, 997–1003.

Salina, D., Bodoor, K., Eckley, D.M., Schroer, T.A., Rattner, J.B., and Burke, B. (2002). Cytoplasmic dynein as a facilitator of nuclear envelope breakdown. Cell *108*, 97–107.

Schatten, G., Simerly, C., and Schatten, H. (1985). Microtubule configurations during fertilization, mitosis, and early development in the mouse and the requirement for egg microtubule-mediated motility during mammalian fertilization. Proc. Natl. Acad. Sci. USA *82*, 4152–4156.

Skibbens, R.V., Skeen, V.P., and Salmon, E.D. (1993). Directional instability of kinetochore motility during chromosome congression and segregation in mitotic newt lung cells: a push-pull mechanism. J. Cell Biol. *122*, 859–875.

Skold, H.N., Komma, D.J., and Endow, S.A. (2005). Assembly pathway of the anastral Drosophila oocyte meiosis I spindle. J. Cell Sci. *118*, 1745–1755.

Sorensen, R.A. (1973). Cinemicrography of mouse oocyte maturation utilizing Nomarski differential-interference microscopy. Am. J. Anat. *136*, 265–276.

Srayko, M., Kaya, A., Stamford, J., and Hyman, A.A. (2005). Identification and characterization of factors required for microtubule growth and nucleation in the early C. elegans embryo. Dev. Cell *9*, 223–236.

Stepanova, T., Slemmer, J., Hoogenraad, C.C., Lansbergen, G., Dortland, B., De Zeeuw, C.I., Grosveld, F., van Cappellen, G., Akhmanova, A., and Galjart, N. (2003). Visualization of microtubule growth in cultured neurons via the use of EB3-GFP (end-binding protein 3-green fluorescent protein). J. Neurosci. *23*, 2655–2664.

Strickland, L., von Dassow, G., Ellenberg, J., Foe, V., Lenart, P., and Burgess, D. (2004). Light microscopy of echinoderm embryos. Methods Cell Biol. *74*, 371–409.

Van Blerkom, J. (1991). Microtubule mediation of cytoplasmic and nuclear maturation during the early stages of resumed meiosis in cultured mouse oocytes. Proc. Natl. Acad. Sci. USA *88*, 5031–5035.

Van Blerkom, J., and Bell, H. (1986). Regulation of development in the fully grown mouse oocyte: chromosome-mediated temporal and spatial differentiation of the cytoplasm and plasma membrane. J. Embryol. Exp. Morphol. *93*, 213–238.

Wassarman, P.M., and Fujiwara, K. (1978). Immunofluorescent antitubulin staining of spindles during meiotic maturation of mouse oocytes in vitro. J. Cell Sci. *29*, 171–188.

Yajima, J., Edamatsu, M., Watai-Nishii, J., Tokai-Nishizumi, N., Yamamoto, T., and Toyoshima, Y.Y. (2003). The human chromokinesin Kid is a plus end-directed microtubule-based motor. EMBO J. *22*, 1067–1074.